Reprinted from

PHYSICS OF THE EARTH AND PLANETARY INTERIORS

Physics of the Earth and Planetary Interiors 86 (1994) 147–164

# Variability of P660s phases as a consequence of topography of the 660 km discontinuity

Suzan van der Lee [a,*], Hanneke Paulssen [b], Guust Nolet [a]

[a] *Department of Geological and Geophysical Sciences, Princeton University, Princeton, NJ 08544, USA*
[b] *Department of Theoretical Geophysics, University of Utrecht, Budapestlaan 4, 3584 CD Utrecht, Netherlands*

Received 18 October 1993; accepted 20 March 1994

ELSEVIER

Physics of the Earth and Planetary Interiors 86 (1994) 147–164

PHYSICS OF THE EARTH AND PLANETARY INTERIORS

# Variability of P660s phases as a consequence of topography of the 660 km discontinuity

Suzan van der Lee [a,*], Hanneke Paulssen [b], Guust Nolet [a]

[a] *Department of Geological and Geophysical Sciences, Princeton University, Princeton, NJ 08544, USA*
[b] *Department of Theoretical Geophysics, University of Utrecht, Budapestlaan 4, 3584 CD Utrecht, Netherlands*

Received 18 October 1993; accepted 20 March 1994

**Abstract**

Records from the broad-band NARS-NL array (deployed in the Netherlands, western Germany and Belgium) have been analyzed for P to S converted phases from the 660 km discontinuity (P660s). No individual seismogram from this array shows a clear P660s phase. Stacks of (up to 113) crosscorrelograms show P660s energy that is weak in comparison with similar stacks elsewhere. Very high amplitude observations of P660s in single seismograms from the same region have been made in a previous study (Paulssen, 1985, Geophys. Res. Lett., 12: 709–712; Paulssen, 1988, J. Geophys. Res., 93: 10489–10500). Such variations may be due to relief on the 660 km discontinuity. In this paper we quantify the effects of different topographies on the time delays, amplitudes, and waveforms of the direct P wave as well as on the P660s converted wave. Synthetic P and P660s waveforms are calculated by applying a Kirchhoff–Helmholtz integration over the wave fields at the 660 km discontinuity interface. For topography on scales of a few hundreds of kilometers, the effects on the P wave are very small compared with those on the P660s phases. Time delays, focused and defocused amplitudes, and waveform distortion of P660s phases influenced by such topography diminish the coherence of P660s in (synthetic) stacks. Our results show that topography of the 660 km discontinuity with dominant scale lengths of a few hundreds of kilometers and variations in depth of $\pm 15$ km to $\pm 25$ km, is consistent with the pattern of P660s observations in single seismograms and stacks.

## 1. Introduction

Earth models exhibit considerable regional differences, including differences in earth structure at depths around 660 km (Nolet and Wortel, 1989; Kennett and Bowman, 1990; Shearer and Masters, 1992). Additionally, very different estimates for the depth and velocity contrast of the 660 km discontinuity have resulted from detailed studies of seismic phases reflected or converted at the discontinuity. These phases are only intermittently observed in both individual seismograms and stacks of (processed) seismograms, with considerable variation in both arrival time and amplitude. For example, Paulssen (1985, 1988) showed several seismograms from the NARS array (Network of Autonomously Recording Seismographs) in western Europe with anomalously high amplitudes for the P660s phase (Fig. 1). Faber and Müller (1984) observed strong energy for S660p phases at the Gräfenberg array (GRF) from American events. Events from eastern Asia

* Corresponding author.


*SSDI* 0031-9201(94)05066-7

produced much less S660p energy at GRF. Lees et al. (1983) noted that reflection coefficients obtained from P'660P' (underside reflections at the 660 km discontinuity) observations are high and difficult to satisfy with mineralogical models. Nakanishi (1986) and Davis et al. (1989) observed P'660P' arrivals intermittently, and where these phases are observed their amplitudes are much larger than predicted by accepted global models such as 1066B (Gilbert and Dziewonski, 1975) or PREM (Preliminary Reference Earth Model; Dziewonski and Anderson, 1981). In a study of NARS intermediate-period data no clear P660P phase could be observed (Wajeman, 1990).

Topography of the 660 km discontinuity has been suggested to explain the intermittency and variations in arrival time and amplitude in observations of the studied seismic phases (e.g. Paulssen, 1988; Davis et al., 1989). A curved discontinuity will cause focusing and defocusing of seismic energy. Shearer and Masters (1992) have derived a topographic map for the smoothed 660 km discontinuity from precursors to SS phases. They concluded that the peak-to-peak variation in the depth of the 660 km discontinuity is no larger than 30 km for the horizontal scales in their study (greater than 1000 km). Bock and Kind (1991) and Richards and Wicks (1990) provided constraints from P to S and S to P converted wave observations of 50 km and 30 km maximum topography, respectively. If the 660 km discontinuity is explained by a phase change (Ito and Takahashi, 1989; Wood, 1990), then lateral variations in depth of the discontinuity could be related to lateral variations in temperature. For example, a temperature change of 600 K would correspond to a 60 km change in depth of the discontinuity. If the chemical composition of the mantle changes across the discontinuity, larger variations in depth can occur (Jeanloz, 1991).

From the unambiguous observations by Paulssen (1985, 1988) of anomalously high-amplitude P660s phases in four seismograms from the NARS array in western Europe (Fig. 1) we estimate amplitude ratios between P660s and P between 16% and 33%. These estimates have some uncertainty owing to receiver effects on the P waveform and coda. Motivated by these observations of anomalously high P660s amplitudes, the portable NARS array was reconfigured, in late 1989, to the situation in Fig. 2 for the NARS-Netherlands (NARS-NL) project. In this configuration we attempted to study the 660 km discontinuity beneath the array in more detail. Most of the NARS-NL stations are located in an area east of NE04/NE15 to minimize microseismic noise originating from the North Sea. A careful study of more than 1.5 years of data from the new configuration (NARS-NL) has been carried out.

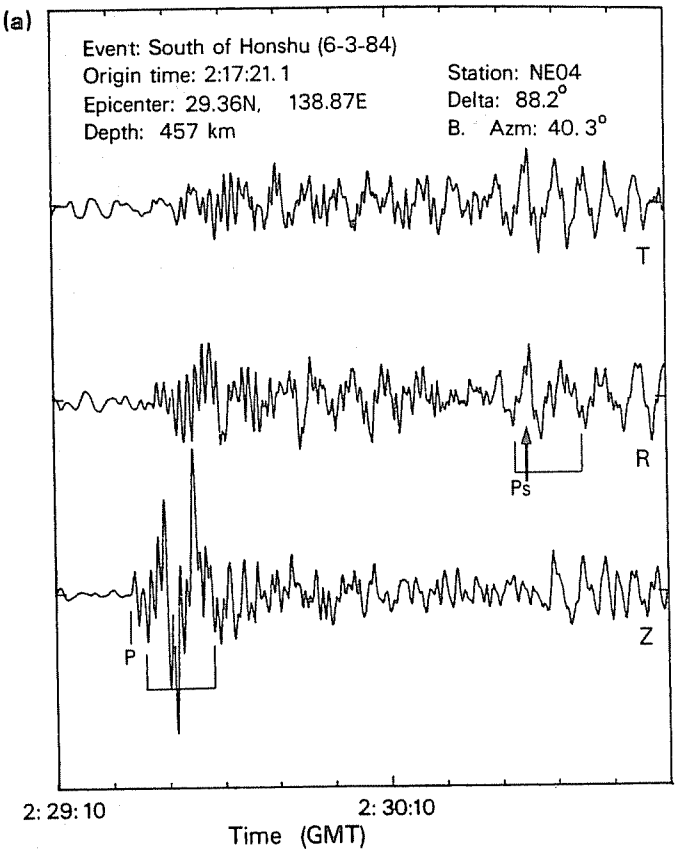


Fig. 1. Seismograms from NARS Stations NE04, NE06 and NE15, showing anomalously high-amplitude P660s phases. Because of the polarization and the arrival time, the identification of this phase as P660s is not in doubt. (a) and (b) after Paulssen (1985, 1988). (c) shows a direct comparison of P waveforms on the vertical component (solid line) and P660s waveforms on the radial component, shifted in time (dotted line). Small differences in the waveforms are to be expected as crustal reverberative processes are different for the incoming P wave and the converted S wave. Comparison with expected crustal responses from Mechie et al. (1983), Matte and Hirn (1988) and Visser and Paulssen (1993) shows agreement between the waveforms before the first reverberatory energy (arrows in (c)).

Surprisingly, this study did not produce additional large-amplitude observations in single seismograms. The source–receiver combinations for which Paulssen (1985, 1988) observed the anomalous P660s phases have not been closely enough approximated in these 1.5 years to allow direct comparisons with single seismograms recorded by NARS-NL.

In this paper we present the new data recorded by the NARS-NL array. Current spherically symmetric Earth models predict the amplitude of P660s phases to be of the order of 5% of the amplitude of the P wave, and generally it is unlikely that we can detect such a phase in the P-wave coda in a single seismogram except in a case of strong focusing of seismic energy. We discuss the results of crosscorrelating and stacking the single seismograms to enhance the P660s phase. These stacks show only very weak P660s energy despite a significant reduction in the noise level. This is in contrast to results from similar observations with the Gräfenberg array (Stammler et al., 1991). Next we present synthetic P660s waveforms, calculated using a Kirchhoff–Helmholtz integral, for a 660 km discontinuity with relief and we quantify the expected effects of topography of the 660 km discontinuity for a series of topography models. Finally, we discuss how the NARS observations can be explained through focusing and defocusing of seismic energy by local topography on the 660 km discontinuity.

## 2. Data and data processing

As P660s arrives approximately 66 s after P, we have analyzed seismograms from the NARS-

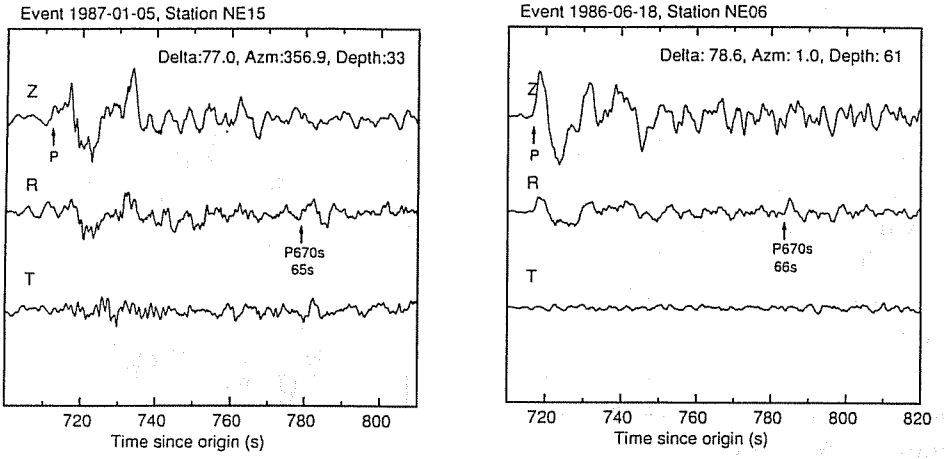


(b)

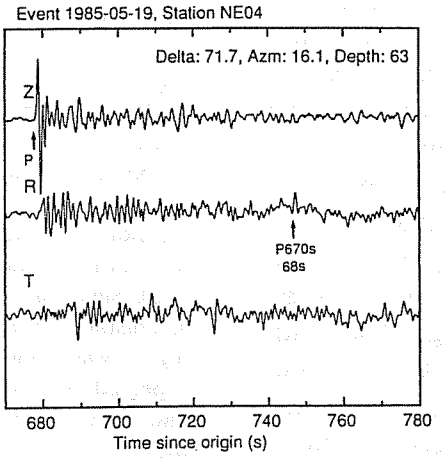


Fig. 1 (continued).

NL array in which we expect no major seismic phase in that time interval. This implies that interference of P660s with phases such as PP and PcP is avoided by choosing the epicentral distance range between 65° and 90°; sP and pP interference with P660s is avoided by choosing the source depth to be larger than 400 km or shallower than 140 km. Any seismogram with a considerable amplitude on the vertical component at the expected P660s arrival time, positively correlated with the radial component, has been discarded, because at these epicentral distances such energy cannot be due to a simple S-wave arrival. Seismograms are only used if there is a clear first P-wave arrival relative to the (microseismic) noise level on both vertical and radial components. Unfortunately, lithospheric structure under the NARS-NL stations can generate reverberatory signals following the P arrival, which are stronger than the actual noise level (see Fig. 4 below), and this might affect the observability of the P660s phase. Using all selection criteria, a total of 113 seismograms have been selected from 19 events for which the locations and azimuthal distribution are shown in Fig. 3.

No unambiguous P660s phase can be identified in the single seismograms selected in this study, indicating that Paulssen's (1985, 1988) observations have a small chance of occurrence.

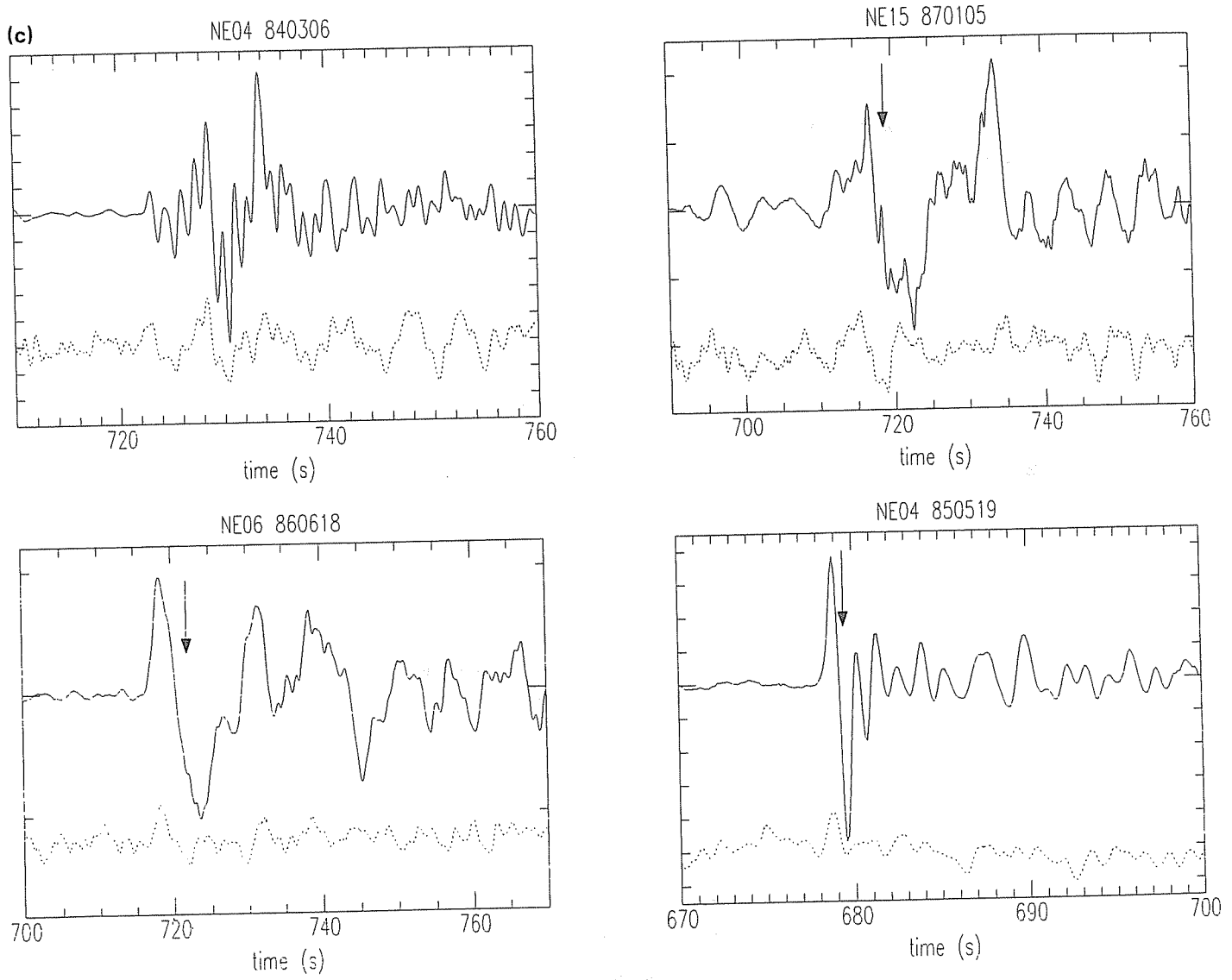


Fig. 1 (continued).

This might indicate a mechanism of focusing in relatively narrow bundles of energy. To investigate the average energy of P660s in the seismograms we have produced slant stacks of crosscorrelograms, following Vinnik (1977), Paulssen (1988) and others. The vertical, radial and transverse components have been crosscorrelated with the P phase from the vertical component. This should enhance P660s, which is expected to be similar to the P waveform for the first several seconds, relative to the noise and reverberative P-coda. The method of crosscorrelation gives very stable results for a fair range of frequencies. The resulting crosscorrelograms for each station are aligned at the P-wave arrival time and have been stacked, using the P-wave slowness. A number of stacks have been produced for slownesses slightly different from the P-wave slowness. Per station stacking over all sources which cover a wide range of azimuths enhances the influence from near-station structure and diminishes the influence of source-side heterogeneities.

## 3. Data analysis

For an epicentral distance of 79° (which is the average epicentral distance from the data used in this study) we expect the P660s wave to arrive with a differential slowness $P_p - P_{p671s}$ of $-0.0017$ s km$^{-1}$, an amplitude relative to the P-wave amplitude of 6.8% and a differential arrival time $T_{P671s} - T_P$ of 69 s for Earth model 1066B. Such predictions should not be taken at face value, as

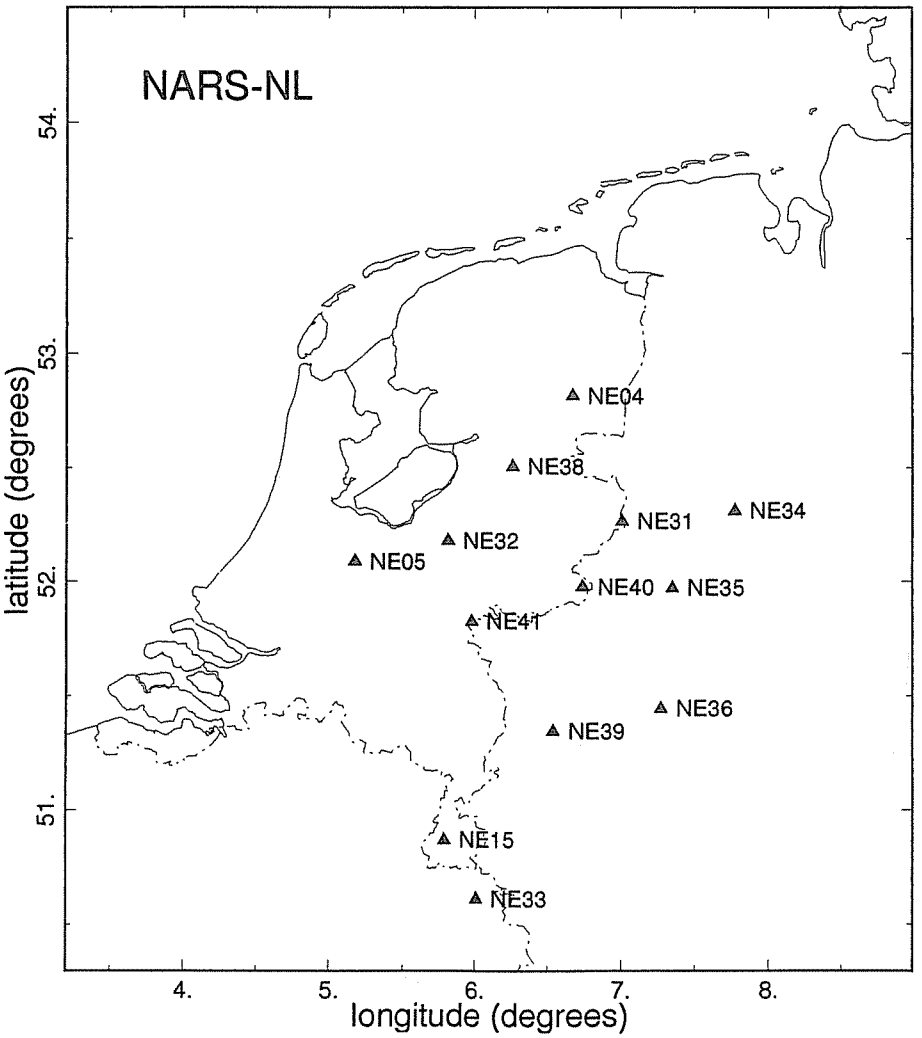


Fig. 2. Configuration of the NARS-NL array.

considerable uncertainty remains about the seismic characteristics of the discontinuity. For example, the IASP91 model for P and S velocities (Kennett and Engdahl, 1991) combined with densities above and below 660 km of 4.08 g $cm^{-3}$ and 4.36 g $cm^{-3}$ (from 1066B values) gives $-0.0011$ s $km^{-1}$, 3.7% and 66.3 s, respectively. As the P660s wave arrives almost vertically, it is expected to show the largest energy on the radial component and only very little energy of opposite sign on the vertical component. As a typical example we shall discuss the data processing for the records of Station NE31. Fig. 4 shows 17 original seismograms, aligned on the P-wave arrival time. Fig. 5 shows the corresponding slant stacks of correlograms. The black areas above and below the actual stack in Fig. 5 are proportional to twice the standard deviation of the stacked correlogram values.

Figs. 4 and 5 are typical for all NARS-NL stations in the sense that no unambiguous P660s arrival can be observed where it is expected (arrow in Fig. 5(b)) in individual seismograms and in the stacks. On the radial component we do observe peaks at 62 and 66 s for differential slownesses $dp$ of $-0.00100$ to $-0.00125$ s $km^{-1}$ which are larger than zero at the 95% confidence level and might be related to the P660s phase. However, the peaks are not significantly larger than other peaks in the stacks where no coherent seismic phase is predicted. Also, there is a peak on the vertical component which is not far out of phase with the peak at 67 s on the radial component, which indicates that the energy arriving near this time is not an S wave coming in at steep angle of incidence. The transverse component shows peaks around the theoretical P660s time and slowness of almost the same order of magnitude as those


Fig. 3. Distribution of selected events (circles) and four events previously studied by Paulssen (1988) (squares).

in the relevant time–slowness interval on the radial component. This indicates that if the energy observed in this interval corresponds to a P660s phase, the 660 km discontinuity must have an extreme topography. Another explanation is that P660s is simply not observed above the reverberatory background noise in the seismogram. As it is higher than the noise level before the first P-wave arrival, the seismic energy in this time window is largely signal or signal-related. This requires further investigation of the NARS-NL records and of possible effects of lateral heterogeneity on the observation of P660s (see Section 4).

In the next step, all seismograms of all NARS-NL stations have been combined into a single stack. Fig. 6 shows stacks of the 113 crosscorrelograms in this data set. The NARS-NL array is roughly 300 km wide and for an array of this size the differential slowness of P660s is for practical purposes the same for all event–station pairs. If the 660 km discontinuity is assumed to be flat we expect features that are consistent over the size of the array to be enhanced, whereas near-source and lower-mantle effects, as well as station site effects, are assumed to average out. However, the stacks of all 113 seismograms do not show an unambiguous P660s arrival either. The small possible converted phase at the arrow in Fig. 6(b) has an amplitude of only 2.3% of the P-wave amplitude, which is matched by many other phases in this plot, is only half of the value predicted with the IASP91 Earth model and does not exceed a 95% confidence level. In stacks of a comparable number of seismograms (170) from the 100 km wide Gräfenberg array, Stammler et al. (1991) observed a more pronounced P660s phase with an amplitude that is more than 20% higher and a lower level of signal-generated noise. Attempts to obtain a pulse with a significant signal-to-noise ratio by stacking subsets over nearby stations were also unsuccessful. This indicates that there is a difference in the characteristics of the 660 km discontinuity for the regions sampled by the NARS-NL array and the Gräfenberg array and in the lithospheric structure beneath the arrays, which generates the reverberatory signals.

Although clear and undisputable high-ampli-

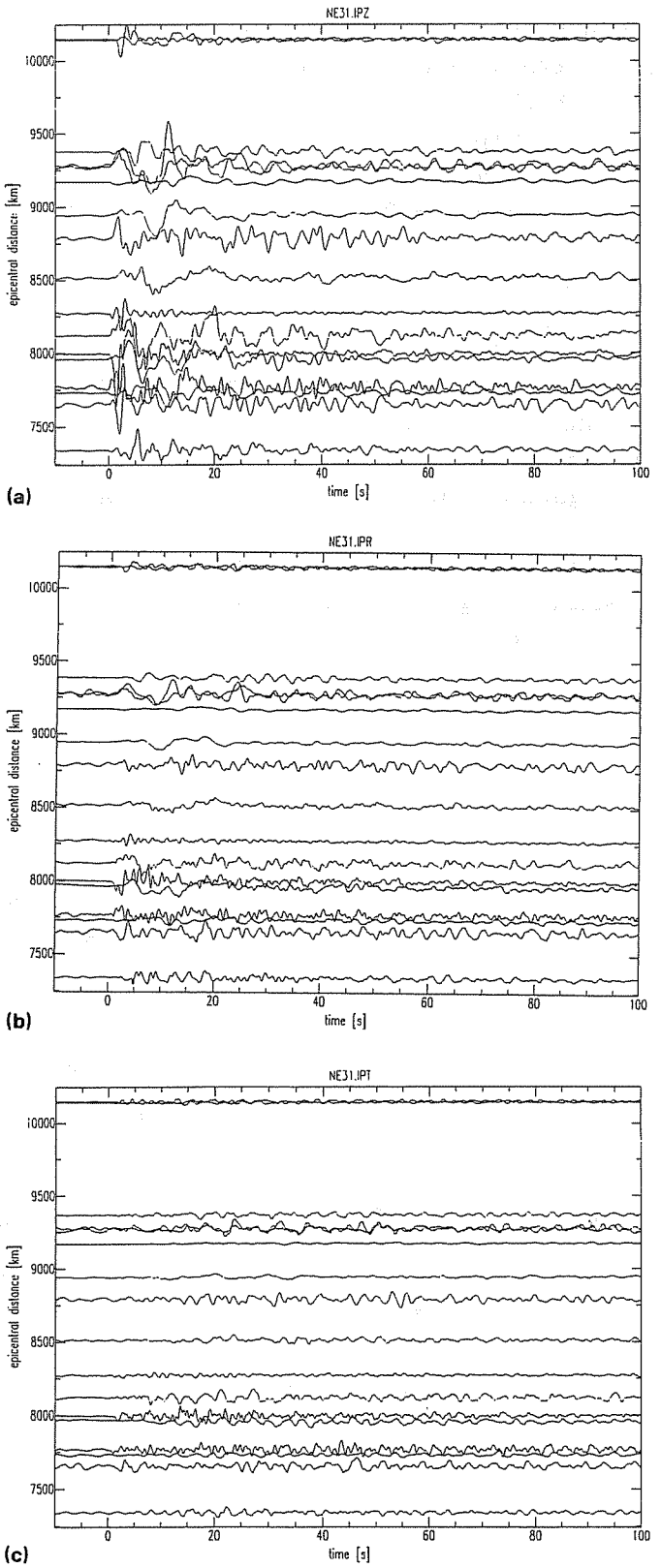


Fig. 4. Original three-component ((a) $Z$ (vertical); (b) $R$ (radial); (c) $T$ (transverse)) seismograms from Station NE31. Seismograms are scaled with their maximum values on the $Z$ component and shifted so that the P-wave arrival times are set to zero.

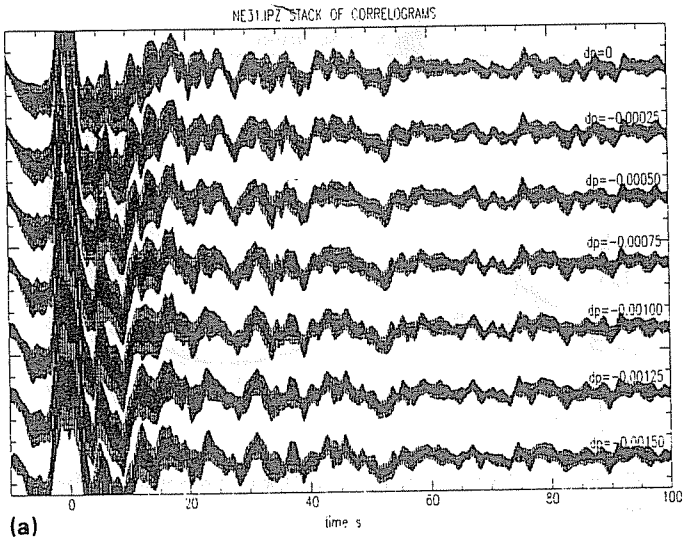


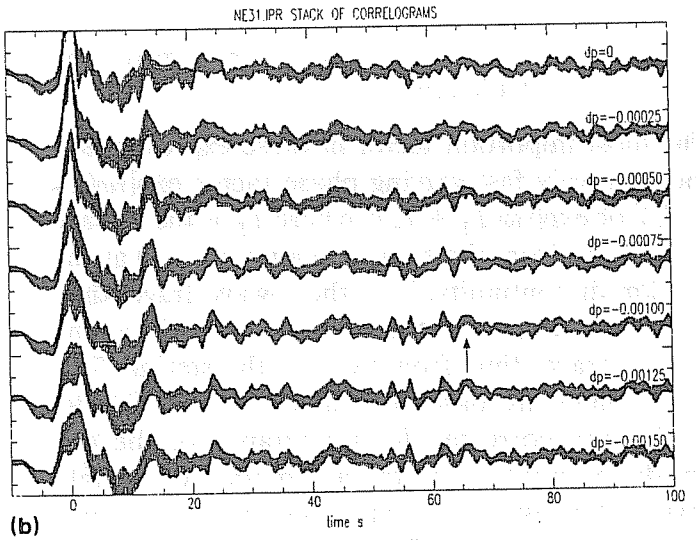


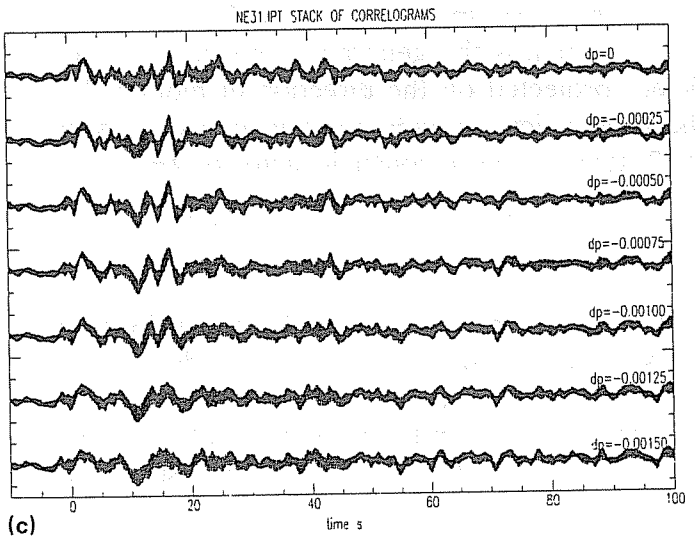


Fig. 5. Stacks of 17 correlograms for seven differential slownesses d$p$ (difference with P-wave slowness in s km$^{-1}$) for Station NE31. The black areas around the curves show the interval between $-2$ and $+2$ times the standard deviation in the stacks. The P660s phase is expected around the arrow. (a) $Z$ (vertical) component; (b) $R$ (radial) component; (c) $T$ (transverse) component.

tude P to S conversions from the 660 km discontinuity have been observed for the region, the data from the NARS-NL array fail to show consistent arrivals of P to S converted waves. Our hypothesis is that lateral heterogeneity in the form of relief on the 660 km discontinuity can reduce the coherence of P660s energy in the stacked seismograms. Focusing and defocusing of P660s energy by such topography of the 660 km discontinuity would explain the few high-amplitude observations by Paulssen (1985, 1988) as well as the weak observations in this study. We shall test this hypothesis in the next sections.

## 4. Synthetic P660s waveforms

To study the effect of the topography of the 660 km discontinuity on the P660s phase in a seismogram we compare calculated waveforms for the P660s phase which have been converted at a (locally) flat 660 km discontinuity with those converted at a 660 km discontinuity with relief. The waveforms are computed using a Kirchhoff–Helmholtz approach. We apply the Multifold Path Integral of Frazer (1987) to the problem of P to S conversion at the 660 km discontinuity. For reference, the regular P wave is computed in the same way as a P660p conversion. For a P to S conversion the (relative) wave field $\boldsymbol{u}^{\mathrm{Ps}}$ at the station is expressed, in the frequency domain, as the sum over the contributions to the wavefield $\boldsymbol{u}^{\mathrm{Ps}}$ from each point $(x,y)$ (i.e. secondary source) at the surface $\Sigma$ of the discontinuity:

$$\boldsymbol{u}^{\mathrm{Ps}}(\omega) = i\omega \int_{\Sigma} \frac{C(x,y)^{\mathrm{Ps}}}{G(x,y)^{\mathrm{Ps}}} \exp\left[i\omega(T_{\mathrm{P}} + T_{\mathrm{s}})\right] \quad (1)$$

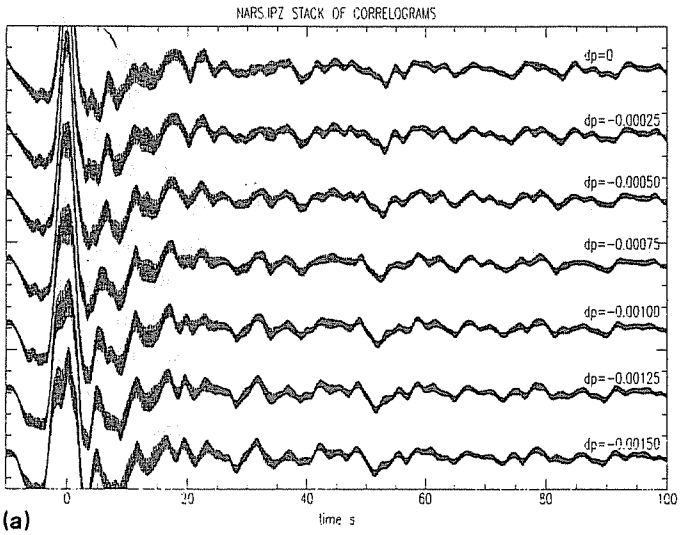


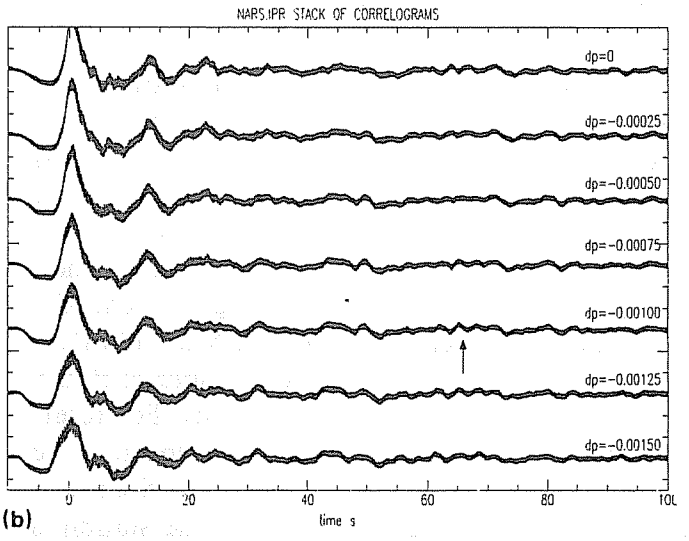


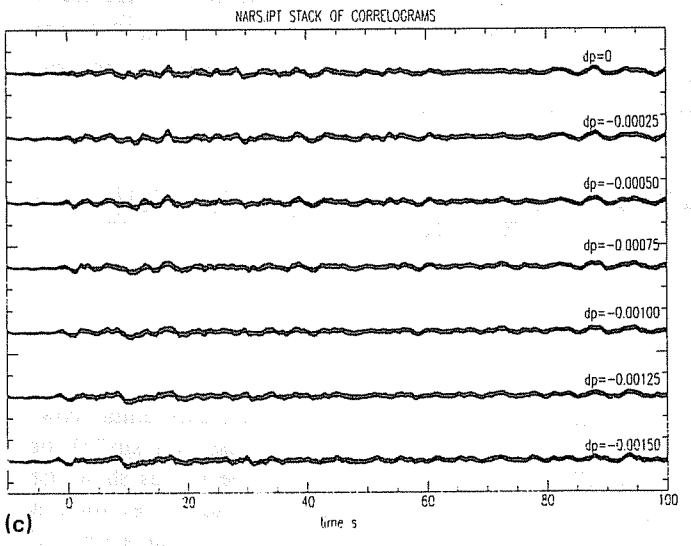


Fig. 6. The same as Fig. 5, but stacks are made of 113 seismograms from all selected events and NARS-NL stations.

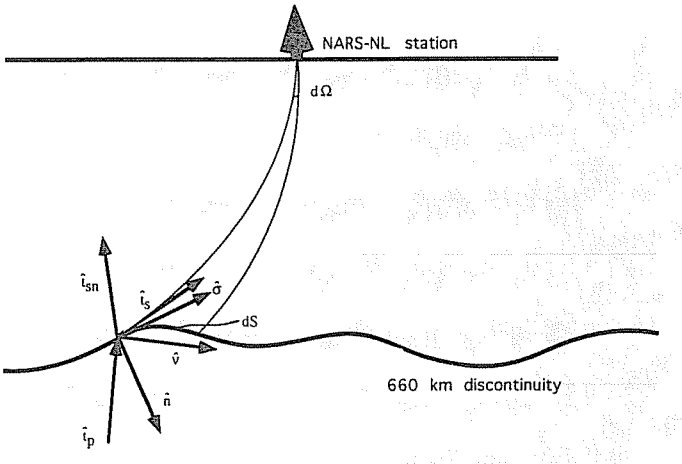


Fig. 7. Geometrical situation at the 660 km discontinuity for an arbitrary ray.

and likewise for the P wave:

$$\boldsymbol{u}^{\mathrm{Pp}}(\omega) = i\omega \int_{\Sigma} \frac{C(x,y)^{\mathrm{Pp}}}{G(x,y)^{\mathrm{Pp}}} \exp\left[i\omega(T_{\mathrm{P}} + T_{\mathrm{p}})\right] \quad (2)$$

The most important factor in these expressions is the relatively fast varying phase factor $\exp[i\omega(T_{\mathrm{P}} + T_{\mathrm{s}})]$ or $\exp[i\omega(T_{\mathrm{P}} + T_{\mathrm{p}})]$, where $T_{\mathrm{P}}$ is the P-wave travel time from the source to a point $(x,y)$ at the 660 km discontinuity, $T_{\mathrm{s}}$ is the S-wave travel time from that point to the station, and $T_{\mathrm{p}}$ is the P-wave travel time from $(x,y)$ to the station. The travel times are based on values for the IASP91 model and corrected for topography of the 660 km discontinuity, with the assumption of straight rays and constant velocities just below and just above the interface. The contribution from each point on the discontinuity is weighted by one over the geometrical spreading factor $G(x,y)$ and by $C(x,y)$, which is the generalized conversion coefficient projected on the direction of motion. For the geometrical spreading factor we use (Frazer, 1987) (leaving out a constant factor of $4\pi$)

$$G(x,y) = \left(\frac{\rho_0 c_0}{\rho_{660} c_{660}}\right)^{1/2} c_{660} \left(-\hat{n}\cdot\hat{t}_{\mathrm{s}} \frac{\mathrm{d}S}{\mathrm{d}\Omega}\right)^{1/2}$$

where $\rho_0$ and $c_0$ are the density and velocity at the surface and $\rho_{660}$ and $c_{660}$ are the density and velocity just above the 660 km discontinuity. The dependence of $G$ on the position $(x,y)$ is through $\mathrm{d}S/\mathrm{d}\Omega$, which is the ratio of the intersection of the discontinuity and a ray tube which has solid

angle $d\Omega$ at the receiver site (see Fig. 7). The inner product $-\hat{n}.\hat{t}_s$ projects the surface area $dS$ to become perpendicular to the rays in the tube. For the generalized conversion coefficient we use, (Frazer, 1987)

$$C^{Ps}(x,y) = A^{Ps}(\hat{n})\left[(\hat{v}\cdot\hat{n})(\hat{t}_{sn}\cdot\hat{b}_s) + (\hat{v}\cdot\hat{t}_s)(\hat{n}\cdot\hat{b}_s) + (\hat{n}\cdot\hat{t}_{sn} + \hat{n}\cdot\hat{t}_s)(\hat{v}\cdot\hat{b}_s)\right]\hat{b}_{so} + A^{Ps}(\hat{n})\left[(\hat{v}\cdot\hat{n})(\hat{t}_{sn}\cdot\hat{c}_s) + (\hat{v}\cdot\hat{t}_s)(\hat{n}\cdot\hat{c}_s) + (\hat{n}\cdot\hat{t}_{sn} + \hat{n}\cdot\hat{t}_s)(\hat{v}\cdot\hat{c}_s)\right]\hat{c}_{so}$$

$$C^{Pp}(x,y) = A^{Pp}(\hat{n})\left[(\hat{t}_{sn_p}\cdot\hat{n}) + (\hat{n}\cdot\hat{t}_{s_p})\right] \times \frac{\lambda(\hat{t}_{sn_p}\cdot\hat{t}_s) + 2\mu}{\lambda + 2\mu}\hat{t}_{so_p}$$

where $A^{Ps}(\hat{n})$ and $A^{Pp}(\hat{n})$ are the P to s and the P to p conversion coefficient according to Aki and Richards (1980). Fig. 7 shows the geometrical situation at the 660 km discontinuity for a P to S conversion for an arbitrary incoming P ray. The unit vector $\hat{t}_s$ is tangent to the S ray leaving a point $(x,y)$ at the 660 km discontinuity towards the receiver and it has a normal and binormal in $\hat{b}_s$ and $\hat{c}_s$. Similarly, $\hat{t}_p$ is the unit vector tangent to the incoming P ray and $\hat{t}_{so}$ is the unit vector tangent to the S ray coming in to the station at the surface. The unit vector $\hat{t}_{sn}$ is tangent to the S ray which would be excited by the incoming P wave according to Snell's law. The unit vector $\hat{n}$ is the normal of the interface of the 660 km discontinuity. With

$$\boldsymbol{\sigma} = \hat{t}_p - (\hat{t}_p\cdot\hat{n})\hat{n}, \qquad \hat{\sigma} = \frac{\boldsymbol{\sigma}}{\|\boldsymbol{\sigma}\|}$$

the unit vector $\hat{v}$ is defined as

$$\hat{v} = (\hat{t}_{sn}\cdot\hat{n})\hat{\sigma} - (\hat{t}_{sn}\cdot\hat{\sigma})\hat{n}$$

It is the component of the incoming P motion that excites the S wave at the 660 km discontinuity (Frazer and Sen, 1985). For the upper-mantle P segments (in the case of a P to P conversion) the vectors $\hat{t}_{s_p}$, $\hat{t}_{sn_p}$ and $\hat{t}_{so_p}$ are the analogs to the $\hat{t}_s$, $\hat{t}_{sn}$ and $\hat{t}_{so}$ vectors for upper-mantle S segments (in the case of a P to S conversion).

Synthetic waveforms are obtained by performing the integrations (1) and (2) over the interface between lower and upper mantle (i.e. the 660 km discontinuity). For each 8 km × 8 km surface segment the integrals are computed analytically, after approximating $G(x,y)C(x,y)$ and $T_P + T_s$ and $T_P + T_p$ by first-order Taylor expansions. The contributions from all surface segments are summed, for 64 frequencies up to 2 Hz. Then the spectrum is inverse fast Fourier transformed and convolved with a reference waveform with a dominant period of 10 s, which is close to the average of the dominant periods of the P waveforms in the data (ranging from 2 to 17 s with an average of 7 s).

For a flat 660 km discontinuity the interference of the contributions from all parts of the discontinuity surface is such that it is destructive everywhere except for the contribution from the zone around the point where Snell's ray has its conversion point, which is the point of stationary phase. For a curved discontinuity surface, the interference pattern changes and the form of the P660s phase can change considerably; several points of stationary phase can coexist, which results in several distinct and/or interfering arrivals. By using (1) we can compare synthetic P660s waveforms for various topographies of the 660 km discontinuity with a reference P660s waveform for a flat 660 km discontinuity. By using (2) we can relate the P660s phases to corresponding P phases and hence produce synthetic crosscorrelations and their stacks.

At this point, we would like to know which type of topography with what size can possibly explain the main characteristics of the pattern of observations of P660s phases, i.e. both a few exceptionally large P660s amplitudes and an overall underestimation of the P660s amplitude as observed in the NARS-NL project. The curvature of the topography determines how the waves are focused and defocused. The curvature could be modeled for instance by a cosine with half-wavelength $W$ and amplitude $A$. A focusing topography is to first order parabolic, indicating that the focusing factor does not change if $A/W^2$ is kept the same. The relationship between $W$ and the period of P660s is somewhat more complicated.

For example, a 3 s P660s has a Fresnel zone of approximately 150 km; this is only half the size of the Fresnel zone for a 10 s P660s. Generally, because our model of topography will not be perfectly parabolic, the area of curvature responsible for focusing is much smaller than the Fresnel zone and the focusing effect is thus similar for both periods. However, for defocusing, the structure over the full Fresnel zone determines if a P660s arrives as one phase or several smaller phases.

We have studied the effects of two different types of models for the topography of the 660 km discontinuity: a single smooth ramp in the depth of the 660 km discontinuity and an egg-box-like 660 km discontinuity.

## 5. Synthetic results

Figs. 8 and 9 show examples of the two types of topography, i.e. a ramp and an egg-box. For both topography models we used maximum variations in depth of $\pm 15$ km, consistent with results of Davis et al. (1989), Richards and Wicks (1990), Bock and Kind (1991) and Shearer and Masters (1992). The dominant width $W$ of the topography is varied to study the dependence of the waveforms on the wavelength (scale) of the topography. When the topography of the 660 km discontinuity is flat, Eqs. (1) and (2) both give a delta pulse. After convolution we obtain a reference P waveform and a reference P660s waveform. These are calculated for each of the 113 event–station configurations from the data-set. For each topography model for the 660 km discontinuity another set of 113 synthetic P and P660s waveforms is obtained. These are compared with the reference waveforms and combined into a stack of crosscorrelograms, in the same way as the data have been stacked. Reference stacks are constructed from the reference waveforms. The stacks are made for differential slowness $dp = -0.0010$ s km$^{-1}$. This value is slightly less than the value predicted

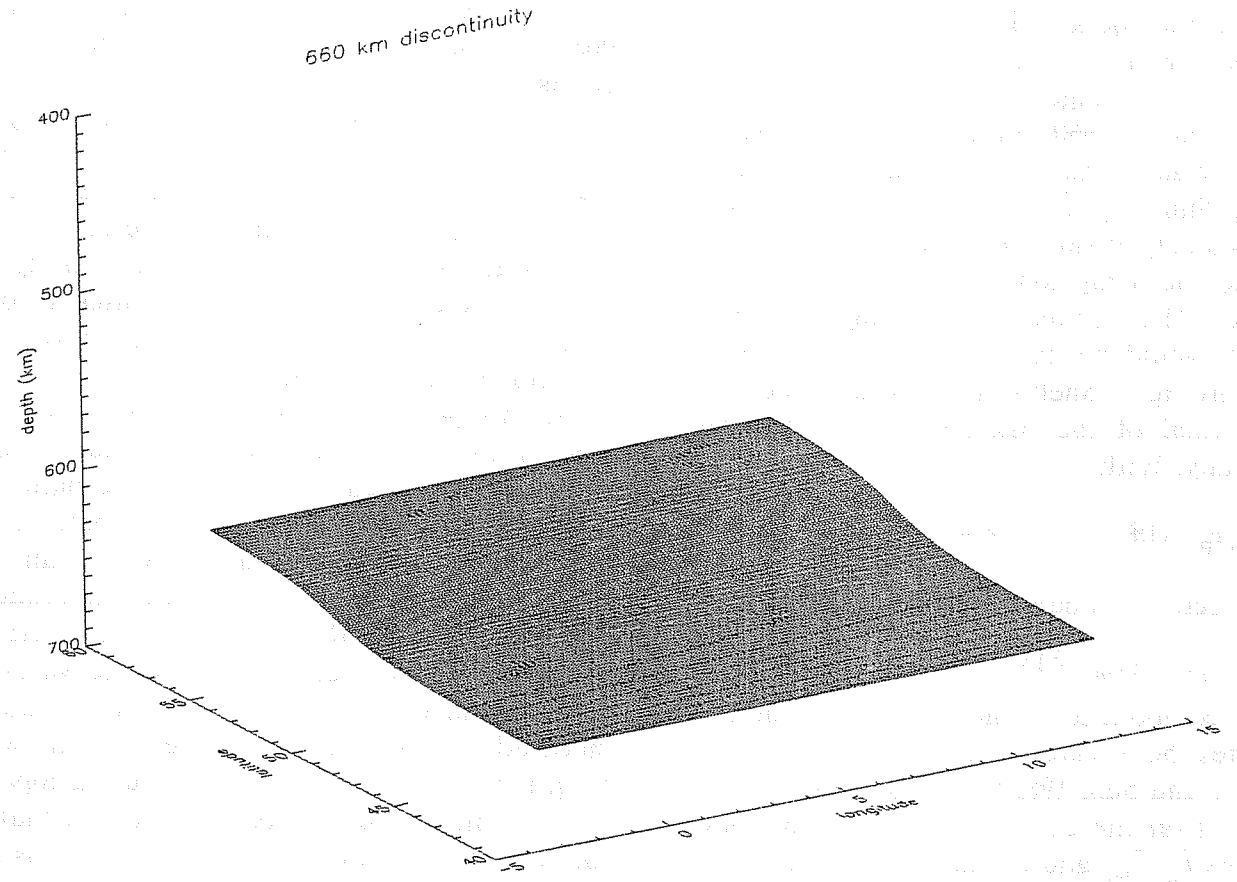


Fig. 8. Ramp model for topography of the 660 km discontinuity. The depth level of the discontinuity smoothly increases 30 km going from north to south, $W = 200$ km.

for the average epicentral distance, because the median epicentral distance for the 113 NARS-NL event–station configurations is slightly higher than the average epicentral distance. The conversion coefficient obtained for this stack is consequently also slightly less than the predicted 3.7% for the average epicentral distance, and has a value of 3.5%. As the stacks are constructed from synthetic seismograms without noise or other seismic phases than P660s and P, a qualitative comparison with the data stacks (Figs. 5 and 6) is not very informative. Of interest here is the quantitative comparison of the amplitude of P660s in the synthetic stacks and the data stacks.

For both topography models the P waves are less affected by the topography than the converted phases. This is not unexpected, as the velocity contrast between the P-wave velocities across the discontinuity is much smaller than the contrast between the P velocity just below and the S velocity just above the discontinuity and therefore the P rays are much less refracted. Also, the Fresnel zone of the P wave at the discontinuity is much larger than the Fresnel zone for P660s so that the P waveform is much less affected by variations in depth of the discontinuity. However, slight deviations in the P waveform can make a small contribution to the amplitude in the stack of crosscorrelograms of P and P660s. First we will discuss the effects of the ramp model. We are interested in such a discontinuity because it might serve as a model for a transition from the mantle beneath an old craton (such as Scandinavia) towards the mantle beneath younger lithosphere. Or, for example, it might also represent a boundary between a subducted slab and surrounding mantle.

The ramp topography model (Fig. 8) is defined by depth $z = 660 + (2A/\pi)\arctan(2x/W + 1)$. Where $A = 15$ km and $x$ is in kilometers from the center of the NARS-NL array, the positive direction is defined as the south direction. Fig.

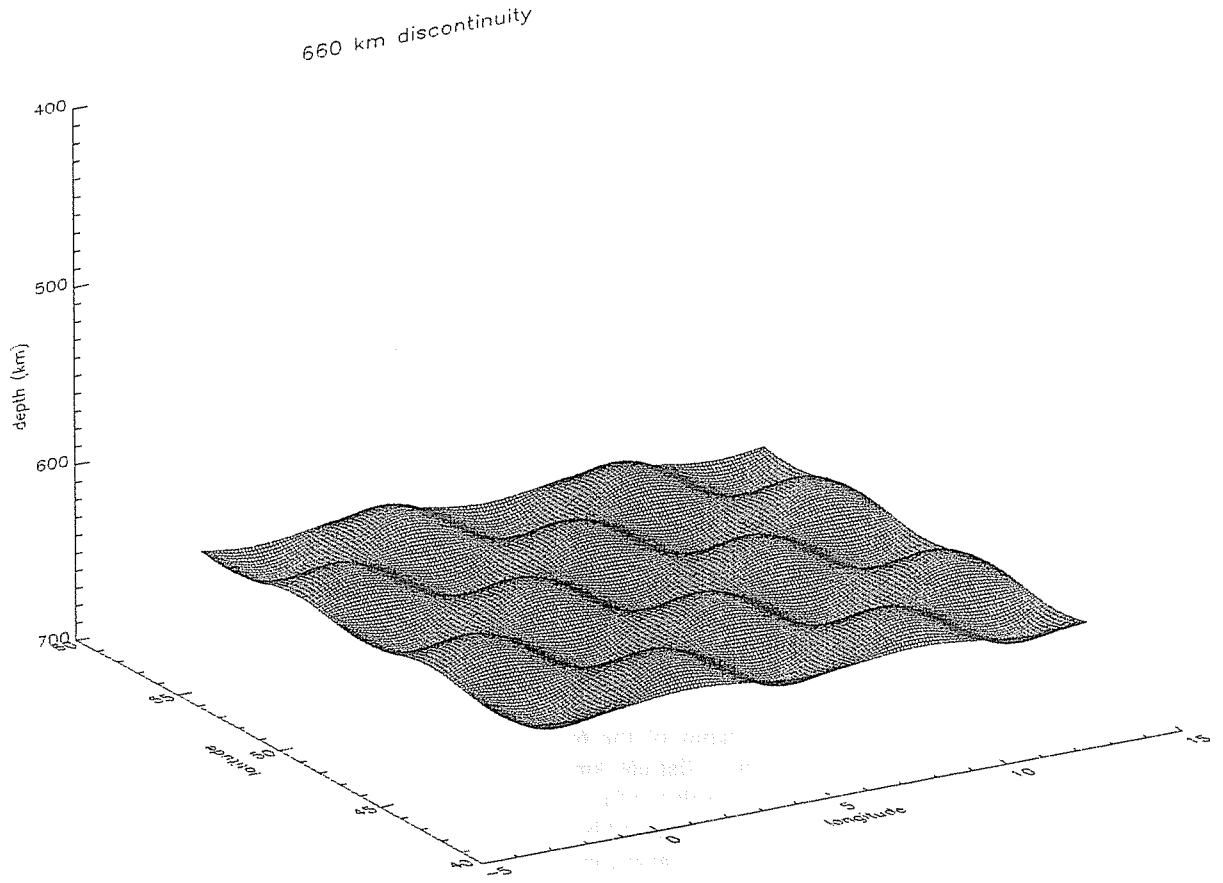


Fig. 9. Egg-box model for topography of the 660 km discontinuity. Topography is centered at the midpoint of the NARS-NL array, $W = 300$ km, $A = 15$ km.

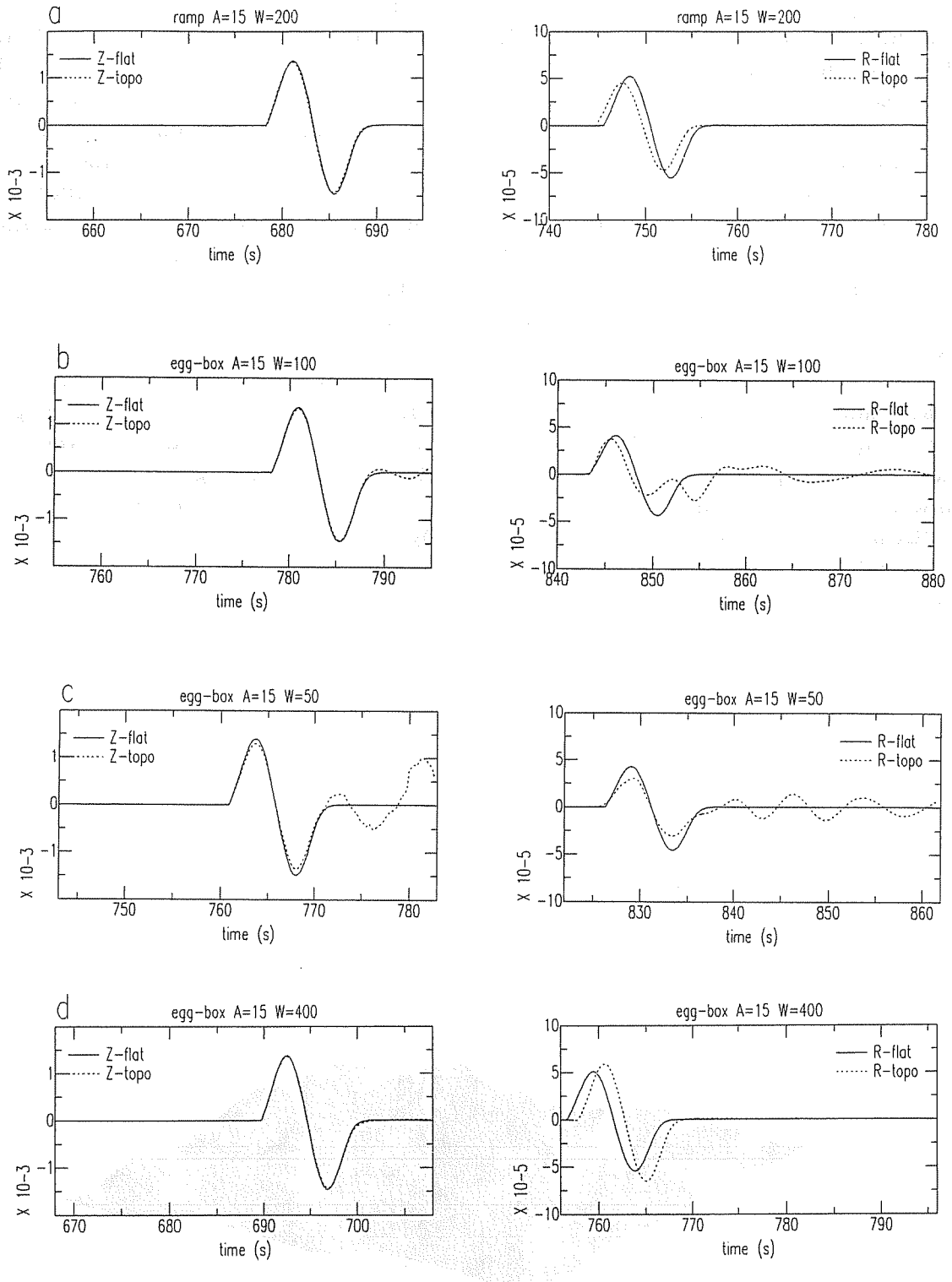


Fig. 10. Examples of waveforms affected by topography of the 660 km discontinuity. Solid and dashed lines are identified by component ($Z$, vertical; $R$, radial; $T$, transverse) and a flat 660 km discontinuity (flat) vs. a 660 km discontinuity with topography (topo). The topography type is given in the title, with values of amplitude $A$ and half-wavelength $W$. The examples are computed for different event–station pairs taken from the real data. Listed below are station name, epicentral distance ($\Delta$) and back-azimuth ($\alpha$) for which the shown examples are computed. (a) The ramp topography as shown in Fig. 8. Station NE31, $\Delta = 72°$, $\alpha = 350°$; (b) Station NE32, $\Delta = 91°$, $\alpha = 253°$; (c) Station NE15, $\Delta = 87°$, $\alpha = 49°$; (d) Station NE15, $\Delta = 74°$, $\alpha = 28°$; (e) Station NE34, $\Delta = 92°$, $\alpha = 254°$; (f) imaginary station in center of array and egg-box centered at conversion point; (g) Station NE31, $\Delta = 82°$, $\alpha = 276°$; Station NE33, $\Delta = 83°$, $\alpha = 277°$.

we choose $A = 15$ km. Fig. 9 shows this model for $W = 300$ km. In general, for this type of model the P waveforms are barely affected by the topography. P waveform distortion is only visible for small values of $W$. An example of a small effect on the P waveform is given in Fig. 10(b). The shape and amplitude of the basic P waveform has not changed but there is a small tail after the first arrival. When $W$ increases the coda vanishes. The effect of this topography type is much stronger for the P660s waveform (Fig. 10b). The P660s amplitude has clearly decreased owing to defocusing and interference with arrivals from secondary points of stationary phase. Fig. 10(c) shows waveforms for a value of $W$ of 50 km. It is obvious that effect of defocusing with waveform distortion and secondary arrivals is strong for small values of $W$; going to larger values this effect vanishes. For $W = 400$ km, for example, there is little difference between the waveforms and the reference waveforms for a flat discontinuity (Fig. 10(d)). However, for $W = 400$ km, we have observed some variations in the P660s amplitude in the range from 0.7 to 1.3 times the reference amplitude. Higher increases of the P660s amplitude, up to a factor 1.7 higher, are found for some configurations around $W = 200$ km (Fig. 10(e)). If we increase $A$ to 25 km, and change $W$ accordingly to 260 km, we find a focusing factor of 2.2 (Fig. 10(f)). For the 1066B model this factor is 2.3; multiplied by the P660s conversion coefficient of 7%, it predicts a P660s to P amplitude ratio of 16%, which is significantly higher than the expected ratio. Such focusing factors, together with an amplification effect for horizontal motion in the top sedimentary layer, allow us to explain the high-amplitude observations by Paulssen (1985, 1988). Likewise, the topography model seems to explain the energy we observe on the transverse components (see Figs. 1 and 4). Synthetic P660s waveforms for the transverse component show a considerable energy content, up to 60% of the energy of the radial component for $W \approx 100$ km and up to 20% of the radial component energy for $W \approx 300$ km. Examples are shown in Fig. 10(g).

It is clear that the calculated behaviour of P660s waveforms as a consequence of topography

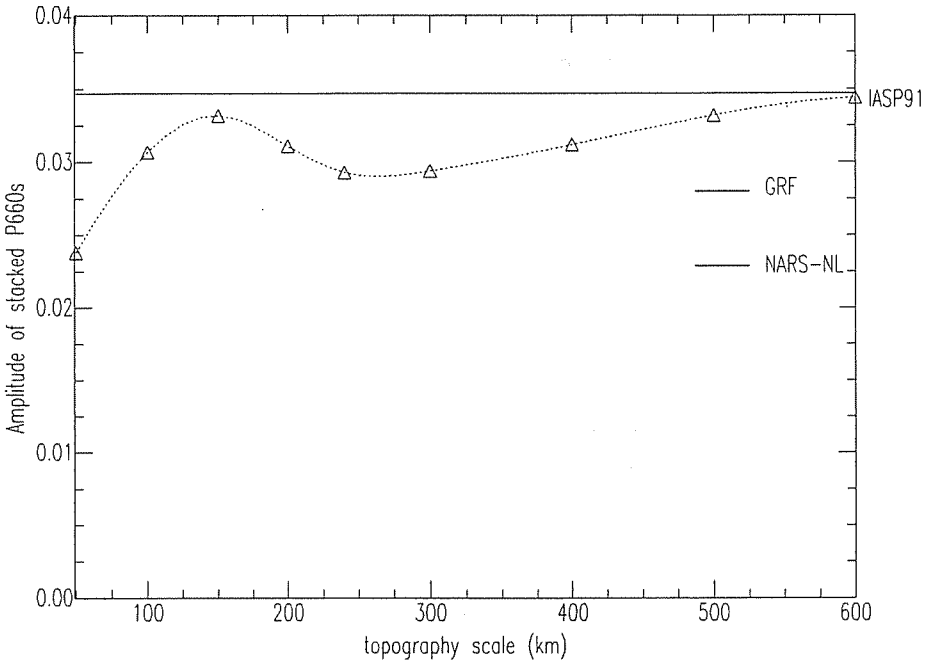


Fig. 11. Amplitude of P660s in a stack of synthetic crosscorrelograms as a function of the scale of topography ($W$) of the 660 km discontinuity. The topography is an egg-box with $A = 15$ km. The solid line is the reference P660s amplitude (percentage of the P-wave amplitude) for IASP91; the dashed line is a spline interpolation through the P660s amplitudes of synthetic stacks (triangles). Also indicated are the value levels found from stacks of data from the GRF (Stammler et al., 1991) and NARS-NL array, respectively. Their difference is of the order of the standard deviation for the NARS-NL value (Fig. 6(b)).

of the 660 km discontinuity will have considerable effect on the amplitudes of P660s in stacks such as those constructed for the data in this study. For several values of $W$ we applied the same processing as done for the data to the synthetic waveforms, for the same station–event pairs. The amplitudes of the P660s in the stacks, relative to the amplitude of the autocorrelation of the P waveform with itself (scaled to unity), is shown in Fig. 11 as a function of $W$. As expected, the curve asymptotically meets the stack amplitude value for a flat topography for large values of $W$. This shows that when $W$ becomes much larger than the Fresnel zone, topography has little effect on the P660s stack amplitude. We expect more scattering, defocusing and destructive interference, and hence a decreasing stack amplitude, as $W$ decreases. Overall, this is clearly the case (Fig. 11), although not for the bulge at $W = 150$ km. We see that the decreasing amplitude trend is partly restored for $W \approx 150$ km, by means of focusing of P660s energy. If $W = 150$ km then the wavelength of the topography is 300 km, which is just the value of the P660s Fresnel zone at 660 km. For topography of this scale we observe the strongest focusing of P660s energy (Fig. 10), which explains the bulge in Fig. 11. However, the stack amplitude of the P660s in the focusing scale range does not exceed the stack amplitude that would occur for a flat discontinuity. This is mainly because if there is focusing of energy to one point, the surrounding (larger) area must contain defocused energy. Fig. 11 allows us to explain some of the apparent absence of a P660s phase in stacks.

Smooth topography such as the egg-box model allows us to explain extraordinary amplitudes of P660s phases as observed by Paulssen (1985, 1988) by focusing of P660s energy. Consequently, in other areas P660s energy is defocused. This could explain the small possible P660s phase as observed in the stacked data. If our topography model were less smooth in certain areas the overall effect from defocusing would become more important relative to focusing; this would result in an even smaller stack amplitude. Therefore a combination topography of a ramp and egg-box with $W \approx 250$ km and "noisier" egg-boxes of both larger and smaller scales will provide a joint explanation of the observations collected in this study. The parameters of such a combination cannot yet be uniquely determined from the NARS-NL data, which have a station separation of the order of 50 km.

## 6. Discussion and conclusion

In this paper we have shown stacks of cross-correlograms from the NARS-NL array which exemplify the erratic character of converted phases at the 660 km discontinuity by showing an absence of unambiguous P660s phases, even though a few stations from the previous configuration of the NARS array have shown anomalously high amplitudes for the P660s phase in unstacked seismograms (Paulssen, 1985, 1988). We have modeled the effect of topography on the 660 km discontinuity on signal amplitude and coherence, and conclude that lateral variation in the depth of the 660 km discontinuity beneath the NARS-NL array can explain the character of all of these observations. We note that lateral heterogeneity in the upper mantle fails to do so because the effects of such heterogeneities on the waveform of P660s is at least an order of magnitude smaller than the effect of a curved 660 km discontinuity, where the effective velocity contrast between P and S velocity is 52%. Neither can we explain the P660s observations discussed in this paper by variations in velocity contrast across the 660 km discontinuity, because such variations are again an order of magnitude smaller. Another factor that could affect the P660s amplitudes is lateral heterogeneity in anelasticity. However, there are no indications of highly attenuative (and hence of low seismic velocity) structure in the upper mantle beneath western Europe (Paulssen, 1987; Stammler et al., 1991; Spakman et al., 1993) except for the low velocity zone (LVZ) around a depth of 200 km. Attenuative effects on the amplitudes of P660s from the LVZ or from, for example, a sedimentary layer in the crust beneath NARS-NL can be estimated (with $Q$ estimates of 80 and 20, respectively) to be of the order of only 10% of the

elastic P660s amplitude. This is again much smaller than the effects of topography of the 660 km discontinuity. Also, the intermittent nature of P660s observations (Paulssen, 1988) rules out that attenuation is an important factor. Another explanation for the observations in this study could be that the noise level in the seismograms is too high to distinguish weak seismic phases from noise. Signal-generated noise can interfere with seismic phases so that crosscorrelation will not enhance these weak phases. However, records showing an excessive (microseismic) noise level, as well as records showing an obvious (scattered) phase other than P660s at the expected arrival time of P660s, have been excluded from the stacks. As a result, the 95% confidence level in the stacks is in general less than the expected amplitude for the P660s phase. We therefore conclude that the noise level is sufficiently low and cannot fully explain the absence of clear P660s.

Therefore we conclude from the synthetic P660s waveforms calculated in this study that topography of the 660 km discontinuity with half-wavelengths $W$ roughly larger than 50 km and not much larger than 500 km, and variations in depths of roughly $\pm 15$ km and occasionally $\pm 25$ km (for values of $W$ roughly over 150 km) may very well explain the large variance in the observations of P660s phases in seismograms. Such topography can focus, defocus and deform the waveform considerably, and can cause arrival time variations of $\pm 2$ s, which also decreases the coherence of the stack. Topography on these scales may be superimposed on larger-scale depth variations such as found by Shearer and Masters (1992). Our results indicate that topography at the large wavelengths as found by Shearer and Masters (1992) does not lead to any noticeable effect (see Fig. 11). For the NARS-NL area they found an almost constant (long-wavelength) depth deviation of less than 4 km. For other 660 km discontinuity converted/reflected phase observations the topography may also play an important role in explaining large variations.

Observations from this study and previous seismological studies (Vinnik, 1977; Faber and Müller, 1984; Paulssen, 1988; Wajeman, 1988; Davis et al., 1989) which are consistent with relief on the 660 km discontinuity are as follows: the intermittency of the observations; the amplitude fluctuations of the observed phases; considerable energy on the transverse component; small arrival time delays and multiple arrivals. A combination of egg-box types of topography, possibly but not necessarily combined with a ramp, having maximum depth variations of $\pm 25$ km over dominant scale lengths of a few hundreds of kilometers, located beneath the surroundings of the NARS-NL array, is a good and plausible explanation of the wide range of characteristics of the P660s phase observed in this region. The scales of topography of the 660 km discontinuity inferred from our analysis are of the order of the Fresnel zone of P660s (300 km) for an incident P wave with a dominant period of 10 s.

If the 660 km discontinuity represents a phase change from spinel to perovskite and magnesiowüstite (Ito and Takahashi, 1989), lateral variations in depth of the 660 km discontinuity may then be related to corresponding variations in temperature and/or pressure. With a pressure–temperature slope of $-4$ MPa $K^{-1}$ (Ito et al., 1990) and a hydrostatic pressure–depth slope of 40 MPa $km^{-1}$ a lateral variation in depth of 30 km could be caused by a lateral variation in temperature of some 300 K. A lateral difference in Mg/Fe ratio can also cause a lateral difference in the depth of the phase change, but this effect is expected to be very small as the dissociation pressure is almost independent of iron content in the range $Fe/(Mg + Fe) < 0.22$, where spinel dissociates into perovskite and magnesiowüstite in an extremely narrow pressure interval (Ito and Takahashi, 1989). For the topography constraints for the 660 km discontinuity from this study, it follows that temperature changes less than 300 K could occur over horizontal distances of few hundreds of kilometers.

## Acknowledgments

The NARS network was funded by the Netherlands Organization for Pure Research (NWO-AWON). Subsequent funding for NARS-NL was obtained from the University of Utrecht,

with partial support from Shell Research. We thank Filip Neele for numerous valuable discussions. During the final stages of this research, Suzan van der Lee was supported under NSF Contract EAR92-04386.

## References

Aki, K. and Richards, P.G., 1980. Quantitative Seismology, Theory and Methods. W.H. Freeman, San Francisco, 932 pp.

Bock, G. and Kind, R., 1991. A global study of S-to-P and P-to-S conversions from the upper mantle transition zone. Geophys. J. Int., 107: 117–129.

Davis, J.P., Kind, R. and Sacks, I.S., 1989. Precursors to P'P' re-examined using broad-band data. Geophys. J. Int., 99: 595–604.

Dziewonski, A.M. and Anderson, D.L., 1981. Preliminary reference Earth model. Phys. Earth Planet. Inter., 25: 297–356.

Faber, S. and Müller, G., 1984. Converted phases from the mantle transition zone observed at European stations. J. Geophys. Res., 54: 183–194.

Frazer, L.N., 1987. Synthetic seismograms using multifold path integrals—I. Theory. Geophys. J.R. Astron. Soc., 88: 621–646.

Frazer, L.N. and Sen, M.K., 1985. KH reflection seismograms in a laterally inhomogeneous multilayered elastic medium —I. Theory. Geophys. J.R. Astron. Soc., 80: 121–147.

Gilbert, F. and Dziewonski, A.M., 1975. An application of normal mode theory to the retrieval of structural parameters and source mechanisms from seismic spectra. Philos. Trans. R. Soc. London, Ser. A, 278: 187–269.

Ito, E. and Takahashi, E., 1989. Postspinel transformations in the system $Mg_2SiO_4$–$Fe_2SiO_4$ and some geophysical implications. J. Geophys. Res., 94: 10637–10646.

Ito, E., Akaogi, M., Topor, L. and Navrotsky, A., 1990. Negative pressure–temperature slopes for reactions forming $MgSiO_3$ perovskite from calorimetry. Science, 249: 1275–1278.

Jeanloz, R., 1991. Effects of phase transitions and possible compositional changes on the seismological structure near 650 km depth. Geophys. Res. Lett., 18: 1743–1746.

Kennett, B.L.N. and Bowman, J.R., 1990. The velocity structure and heterogeneity of the upper mantle. Phys. Earth Planet. Inter., 59: 134–144.

Kennett, B.L.N. and Engdahl, E.R., 1991. Travel times for global earthquake location and phase identification. Geophys. J. Int., 105: 429–466.

Lees, A.C., Bukowinski, M.S.T. and Jeanloz, R., 1983. Reflection properties of phase transition and compositional change models of the 670-km discontinuity. J. Geophys. Res., 88: 8145–8159.

Matte, P. and Hirn, A., 1988. Seismic signature and tectonic cross section of the Variscan crust in western France. Tectonics, 7: 141–155.

Mechie, J., Prodehl, C. and Fuchs, K., 1983. The long-range seismic refraction experiment in the Rhenish Massif. In: K. Fuchs, K. von Gehlen, H. Mälzer, H. Murawski and A. Semmel (Editors), Plateau Uplift. Springer, Berlin, pp. 261–275.

Nakanishi, I., 1986. Seismic reflections from the upper mantle discontinuities beneath the Mid-Atlantic Ridge observed by a seismic array in Hokkaido region, Japan. Geophys. Res. Lett., 13: 1458–1461.

Nolet, G. and Wortel, M.J.R., 1989. Structure of the upper mantle. In: D.E. James (Editor), Encyclopedia of Geophysics. Van Nostrand Reinhold, New York, pp. 775–788.

Paulssen, H., 1985. Upper mantle converted waves beneath the NARS array. Geophys. Res. Lett., 12: 709–712.

Paulssen, H., 1987. Lateral heterogeneity of Europe's upper mantle as inferred from modelling of broad-band body waves. Geophys. J.R. Astron. Soc., 91: 171–199.

Paulssen, H., 1988. Evidence for a sharp 670-km discontinuity as inferred from P-to-S converted waves. J. Geophys. Res., 93: 10489-10500.

Richards, M.A. and Wicks, C.W., 1990. S–P conversion from the transition zone beneath Tonga and the nature of the 670 km discontinuity. J. Geophys. Res., 101: 1–35.

Shearer, P.M. and Masters, T.G., 1992. Global mapping of topography on the 660-km discontinuity. Nature, 355: 791–796.

Spakman W., van der Lee, S. and van der Hilst, R., 1993. Travel-time tomography of the European–Mediterranean mantle down to 1400 km. Phys. Earth Planet. Inter., 79: 3–74.

Stammler, K., Kind, R., Kosarev, G.L., Plesinger, A., Horalek, J., Liu, Q. and Vinnik, L.P., 1991. Broadband observations of PS conversions from the upper mantle in Eurasia. Geophys. J. Int., 105: 801–804.

Vinnik, L.P., 1977. Detection of waves converted from P to SV in the mantle. Phys. Earth Planet. Inter., 15: 39–45.

Visser, J. and Paulssen, H., 1993. The crustal structure from teleseismic P-wave coda. II. Application to data of the NARS array in western Europe and comparison with deep seismic sounding data. Geophys. J. Int., 112: 26–38.

Wajeman, N., 1988. Detection of underside P reflections at mantle discontinuities by stacking broadband data. Geophys. Res. Lett., 15: 669–672.

Wajeman, N., 1990. Observations of PP precursors: variations of the 650 km discontinuity properties beneath northern Siberia. In: XXII General Assembly European Seismological Commision, Program and Abstracts, Generalitat de Catalunya, Barcelona, 17–22 September, SCB.11, 266 pp.

Wood, B., 1990. Postspinel transformations and the width of the 670-km discontinuity: a comment on "Postspinel transformations in the system $Mg_2SiO_4$–$Fe_2SiO_4$ and some geophysical implications" by E. Ito and E. Takahashi. J. Geophys. Res., 95: 12681–12685.